4D force patterning enables spatial control of angiogenesis

Sina Kheiri[1,2†], Jessica Shah[1,3†], Shashaank A. Venkatesh[3], Roger D. Kamm[1,2], Ritu Raman[1,*]

[1] Department of Mechanical Engineering, Massachusetts Institute of Technology, Cambridge, MA, USA

[2] Department of Biological Engineering, Massachusetts Institute of Technology, Cambridge, MA, USA

[3] Harvard-MIT Division of Health Sciences and Technology, Institute for Medical Engineering and Science, Massachusetts Institute of Technology, Cambridge, MA, USA.

[†]These authors contributed equally to this work

*Corresponding Author: Ritu Raman

Email: ritur@mit.edu

Author Contributions: Methodology: S.K., J.S., R.D.K., R.R.; Investigation: S.K., J.S.; Formal Analysis: S.K., J.S., S.A.V.; Visualization: S.K., J.S.; Writing: S.K., J.S., R.D.K., R.R.; Project Administration: R.R.; Funding: R.R.

Competing Interest Statement: The authors declare no competing interests.

Keywords: tissue engineering, vasculature, angiogenesis, mechanobiology, biofabrication

Abstract

Engineering organized microvascular networks remains a critical challenge in tissue engineering and regenerative medicine. While biochemical approaches for patterning angiogenesis via growth factor delivery have shown promise, their inability to pattern sustained growth factor gradients with precise spatiotemporal control limit their effectiveness. Here, we demonstrate that dynamically patterned mechanical forces can provide precise spatiotemporal control over angiogenic sprouting in 3D microvascular networks. We developed a magnetically actuated 3D human vessel-on-a-chip platform that integrates a perfusable endothelialized microchannel within a collagen matrix and allows non-invasive, tunable, multi-axial mechanical stimulation across all three spatial dimensions and time (4D). Using an automated 3-axis actuator, we systematically investigated how strain magnitude, frequency, and direction modulate endothelial cell behavior and vessel morphogenesis. Dynamic mechanical stimulation at physiological strain magnitudes (5–15%) enhanced endothelial alignment and barrier function while promoting angiogenesis in a strain-magnitude–dependent manner: lower dynamic strain (5%) maximized sprout initiation, whereas higher dynamic strain (15%) promoted elongation of individual sprouts. Sequential reorientation of strain direction further reprogrammed sprouting trajectories along X, Y, and Z directions, generating complex 3D microvascular geometries such as L-shaped branches. RNA sequencing revealed mechanically induced transcriptional profiles distinct from unstimulated controls, characterized by coordinated upregulation of angiogenic (VEGFA, FGFR1, PDGFA), mechanotransduction (ANKRD1, ZYX, FOSB), extracellular matrix remodeling (ABI3BP, SPOCK1, COL8A1), and barrier-associated (SERPINE2, P2RY1) genes and pathways. Collectively, these findings establish a strategy for spatiotemporally controlled angiogenesis through engineered mechanical cues and demonstrate that 4D force patterning can program vascular morphogenesis while preserving function. This approach provides a foundation for engineering hierarchically organized vascular networks for tissue regeneration and disease modeling.

Introduction

The vascular network spans a wide range of length scales, from millimeter- to centimeter-scale arteries and veins to microscale capillaries about 5–10 μm in diameter.(1) This hierarchy facilitates the transport of oxygen, nutrients, and signaling molecules while removing metabolic waste.(2) Perfusable vasculature is thus essential for the survival, growth, and integration of engineered tissues, as diffusion limits cell viability to only a few hundred micrometers, leading to hypoxia, necrosis, and loss of function.(3, 4) Yet, replicating the intricate structure and function of native microvasculature remains a significant challenges in tissue engineering.(2) Although significant progress has been made in engineering microvascular networks within tissues, current approaches generally rely on two strategies: self-organization or pre-patterning.(5–7) Self-organization of endothelial cells embedded within hydrogels produces microscale networks with natural topology, but suffers from random connectivity and limited control over network remodeling and evolution. In contrast, pre-patterning of vascular templates via methods like 3D bioprinting provides precise spatial control but is constrained by resolution limitations (typically 100s of μm), preventing the recapitulation of fine-scale vascular hierarchies and spontaneous remodeling.(8, 9) Consequently, fabrication methods that promote the development of hierarchically organized, precisely patterned, and perfusable microvascular networks hold great promise for advancing engineered tissue models for *in vitro* disease modeling and *in vivo* regenerative medicine applications.

Biochemical patterning strategies have been extensively employed to induce vascular formation by stimulating angiogenesis through pro-angiogenic cues, primarily vascular endothelial growth factor (VEGF).(10, 11) Approaches such as functionalized bioinks for controlled VEGF release and aptamer-tethered VEGF photopatterning have enabled partial spatial regulation of sprouting and network formation.(12, 13) Despite these advances, biochemical methods remain limited by the rapid diffusion and short half-life of VEGF, which hinder the establishment and maintenance of stable, localized gradients in three-dimensional (3D) environments. Furthermore, because

angiogenesis is an inherently spatiotemporal process involving phases of growth, regression, and remodeling, static or one-time VEGF delivery often results in irregular and disorganized vascular networks that deviate from native microvascular architecture.(14, 15)

In native tissues, angiogenesis is governed not only by biochemical cues but also by biomechanical signals that regulate endothelial organization, alignment, and function (16–18). Endothelial cells are highly mechanosensitive and continuously exposed to both fluid flow-induced mechanical stimuli (shear stress and cyclic pressure generated by blood flow within vessels) and extracellular matrix (ECM) deformation-induced mechanical stimuli (tensile and compressive stresses generated by tissue movement surrounding vessels) which collectively influence sprouting, alignment, and barrier function.(19) *In vivo,* blood vessels undergo dynamic mechanical stretching from tissue growth and movement, which influence the spatial patterns and orientation of vascular networks, yet these forces remain largely understudied compared to hemodynamic forces.(20) Early work demonstrated that endothelial spheroids cultured on statically stretched collagen gels exhibited directional outgrowth along the axis of strain (21). While this showed that strain can bias sprouting direction, placing spheroids on top of the stretched gel limited direct force transmission to the cells and lacked physiological cell-matrix embedding. To directly apply mechanical forces in the same plane as the cells, later systems delivered uniaxial or biaxial strain to 2D cell monolayers via deformable 2D substrates. These systems revealed that mechanical stretch can influence network elongation (22), cell and cytoskeletal alignment (23, 24), and reorientation in response to changing strain direction.(23) While these studies provided key insights into how 2D endothelial cell monolayers respond to mechanical cues, they did not fully capture the complex spatial architecture, cell-matrix interactions, and mechanical gradients that influence endothelial behavior in native 3D environments.

Recent efforts have begun to address this limitation by incorporating mechanical stimulation into 3D vessel-on-chip platforms. In one approach, 3D endothelialized lumens embedded in fibrin hydrogels were cyclically stretched by deflecting a thin PDMS membrane using negative pressure (25). While this method enabled mechanical stimulation of a 3D tissue, it did not enable precise spatial control of force patterning. Another approach applied strain to endothelial cell-lined microchannels by dynamically stretching a gelatin-based hydrogel perpendicular to the channel axis (26). Although this platform allows for more controlled directional deformation, the hydrogel formulation was optimized for mechanical extensibility rather than biological remodeling, limiting its ability to support angiogenic sprouting. More recently, a PDMS-based stretchable device applied static mechanical stretching to an engineered vessel embedded within a collagen matrix, demonstrating that strain direction significantly influences sprouting behavior (27). Strain perpendicular to the vessel axis promoted angiogenic outgrowth and alignment, while strain parallel to the vessel inhibited sprouting, highlighting the importance of directional mechanical cues in angiogenesis. While these platforms expanded the ability to study mechanical stimulation in 3D vascular tissues, the applied forces remain global and are typically constrained to one or two axes, limiting the ability to deliver spatially patterned, multi-axial strain with high spatiotemporal precision. As such, key questions remain about how multi-axial and dynamically varying mechanical cues applied along the x, y, and z axes regulate angiogenic sprouting and barrier function in 3D tissues. A central challenge in understanding and directing vascular patterning is thus the difficulty of delivering tunable, non-invasive mechanical stimulation in both 3D space and time (4D) to mimic evolving *in vivo* mechanical environments.

To address limitations of conventional mechanical stimulation methods, magnetic stimulation offers a non-invasive means to apply controlled mechanical forces in engineered tissues.(28–30) We have previously established a magnetic matrix actuation (MagMA) platform in which magnetic actuators embedded in an ECM can be non-invasively actuated by an external magnet, enabling precise spatial patterning of forces within an engineered tissue (31, 32). Previous studies leveraging MagMA focused on 1D stretching of cells seeded on top of an actuating hydrogel. Here, we adapted MagMA to enable 3D actuation of a collagen hydrogel containing a 3D perfusable

vascular channel lined with human endothelial cells. To deliver dynamic, multi-axial strain in 4D, we used a motorized 3-axis actuator to control the position, height, and speed of external magnets above the device, enabling spatial and temporal control over strain magnitude, frequency, and direction within the tissue. By tuning strain magnitude, we observed distinct effects on vascular morphology: lower strain increased sprout number, while higher strain promoted elongation of fewer sprouts. Beyond enhancing sprout initiation and elongation along a single axis, our platform enabled sequential multi-directional mechanical stimulation to dynamically reorient 3D sprouting trajectories along X, Y, and Z dimensions over time. This approach revealed that endothelial sprouts could adapt their growth trajectories in response to changing mechanical inputs, generating complex geometries such as L-shaped sprouts. Transcriptomic profiling further demonstrated that dynamic strain activated angiogenic and mechanosensitive gene programs while preserving barrier function. Together, these findings establish a platform for mechanical stimulation of a human vessel-on-a-chip, highlighting the potential for spatiotemporally patterned forces to program 4D morphogenesis of perfusable microvasculature in engineered tissues.

Results

Design and Fabrication of Magnetically Actuated Human Vessel-on-a-Chip Platform

A human vessel-on-a-chip system was engineered to impose controlled, dynamic mechanical strain on an endothelialized microchannel through an integrated magnetic actuation mechanism (Fig. 1). The device was fabricated using a multi-step molding process (***see Materials and Methods***, Movie S1). Briefly, a glass rod was inserted into the device mold to define a central lumen within a type I collagen matrix (Fig. 1A, steps 1–2), and a 3D-printed stamp was used to pattern the gel and generate a slot for reproducibly positioning the magnetic actuator (Fig. 1A, steps 3–4). The magnetic actuator was then embedded adjacent to the channel (Fig. 1A, step 5) and encapsulated with an additional collagen layer (Fig. 1A, step 6). Human umbilical vein endothelial cells (HUVECs) were seeded into the lumen (Fig. 1A, step 7), forming a confluent endothelium within 48 h. The resulting endothelialized microchannels formed continuous, lumenized vessels in 3D, providing a reproducible platform to investigate the effects of controlled mechanical stimulation on angiogenesis. (Fig. 1A, step 8).

Endothelialization of the collagen microchannel produced a continuous vessel with clearly defined cellular organization (Figs. 1B and C). Confocal fluorescence imaging of PECAM-1 (cell–cell junctions) and F-actin (cytoskeleton) showed that HUVECs formed a circular, perfusable lumen with a diameter of 604 ± 42.2 μm within the vessel-on-a-chip platform. After 3 days of culture in media containing 5 ng/mL of VEGF, endothelial sprouts extended from the parent vessel into the surrounding collagen matrix, demonstrating that the platform supports spontaneous angiogenic initiation, as shown in Figure 1C. To impose controlled mechanical strain on the formed vessels, a custom magnetic stimulation system was developed to control actuation of the collagen hydrogel within the device. The system was designed for high-throughput stimulation, with vessel-on-a-chip devices mounted in standard 6-well plates using a custom insert that accommodated up to 3 well plates, or 18 chips in total (Fig. 1D). To dynamically control the movement of the composite magnetic extracellular matrix, a custom 3-axis (X, Y, and Z) linear actuator was constructed to translate a permanent magnet above the plate with controllable distance, speed, direction, and frequency (***see Materials and Methods***). This movement induced both dynamic and static actuation of the embedded magnetic actuator and surrounding collagen matrix, generating uniform strain along the vessel wall. The strain magnitude was tuned by adjusting the magnetic field strength. Quantitative movement tracking analysis of fluorescent beads embedded in the collagen hydrogel at different locations within the chip (Fig. S1B) confirmed that increasing the magnetic field from 250 G to 1,800 G modulated the strain magnitude, as shown in Figs. 1E and S1C. In this study, strain magnitudes of approximately 5% and 15% at the vessel wall (row 2, Fig S1D) were selected as representative physiological conditions (20) to examine the effects of dynamic, spatiotemporally patterned strain on angiogenic responses.

Strain magnitude and frequency regulate endothelial cell-cell junctions, cell orientation, and barrier function

Using our magnetically actuated human vessel-on-a-chip platform, we investigated how both the magnitude and frequency of applied strain regulate endothelial behavior and sprouting morphogenesis (Figs. 2A and S2A). Constructs were stimulated at 5% and 15% strain magnitude, and the role of dynamic loading was examined by applying either dynamic strain at 1 Hz or static strain. The constructs were cultured for 3 days to allow vessel formation, after which mechanical stimulation was applied once per day for 1 h from day 3 to day 6 to assess the cumulative effects of repeated strain exposure under defined spatiotemporal conditions. Notably, our mechanical stimulation led to formation of sprouts with diameters below 10 μm (Fig. S2B). Our magnetic actuation approach thus enables patterning capillary-scale vessels, with most sprouts forming within the 4–10 μm diameter range (Fig. S2C), in contrast to 3D bioprinting methods that generate channels hundreds of micrometers wide (33). Total sprouting increased over the first 4 days and plateaued thereafter (Fig S2D, Movie S2), indicating saturation of the angiogenic response with prolonged mechanical stimulation. Accordingly, subsequent experiments were conducted using stimulation periods within this dynamic growth phase to capture active angiogenic remodeling. All tissues were compared to unstimulated controls. To evaluate the impact of mechanical stimulation, we performed three levels of analysis: quantifying angiogenesis based on cell–cell junction orientation (Fig. 2B-D), functional assessment of vascular barrier function via permeability assays (Fig. 2E-F), sprout magnitude and direction (Fig. 3 and Fig. 4), and changes in gene expression via RNA sequencing (Fig. 5).

Endothelial cell organization was examined using PECAM-1 immunostaining and assessed with *OrientationJ* analysis of cell–cell junction alignment within the parent vessel. Application of 15% dynamic strain (1 Hz) resulted in the highest degree of endothelial cell alignment along the axis of deformation compared with 15% static strain, 5% dynamic strain, and unstimulated control conditions (Fig. 2B-D). Quantitative orientation analysis demonstrated that dynamic strain enhanced endothelial alignment in a magnitude-dependent manner (Fig. 2C). Rose plots of cell–cell junction orientation showed a narrower angular distribution under 15% strain at 1 Hz compared to 5% strain and no-stimulation controls, indicating a higher degree of directional organization. The percentage of cells oriented at 90° increased significantly under 15% dynamic strain relative to both 5% strain and static culture (Fig. 2D). Notably, under static 15% strain conditions, no significant change in junction orientation as compared to unstimulated controls was observed, suggesting that alignment is specifically induced by dynamic mechanical loading in our platform. These findings indicate that dynamic strain promotes directional endothelial organization, with strain magnitude serving as a key regulator of network alignment.

Barrier function of the endothelialized vessels was evaluated by measuring the diffusion of fluorescent 10 kDa and 40 kDa dextran tracers across the vessel wall following established protocols (34, 35). In unstimulated controls, timelapse confocal imaging showed rapid diffusion of dextran into the surrounding hydrogel, whereas vessels subjected to dynamic strain retained fluorescence within the lumen, indicating reduced permeability (Fig. 2E, Movie S3). Quantitative analysis revealed a significant decrease of diffusive permeability for both 10 kDa and 40 kDa dextran in mechanically stimulated tissues. For the 10 kDa tracer, permeability decreased by nearly two-fold across all stimulated conditions, while the 40 kDa tracer showed approximately a 1.5-fold reduction across all stimulated conditions (Fig. 2F). In all stimulated tissues, the 40 kDa tracer consistently exhibited lower permeability than the 10 kDa tracer, consistent with size-dependent transport behavior.(34) We also confirmed that neither the presence of the mechanical actuator nor the stimulation protocol alone altered baseline vascular properties (Figs. S2E and S2F). Together, these findings indicate that dynamic mechanical stimulation enhances endothelial barrier function, independent of strain magnitude under the conditions tested.

Strain magnitude controls angiogenic sprouting direction and magnitude

Mechanical stimulation induced distinct changes in sprouting architecture, as indicated by the merged fluorescence images of nuclei (yellow), PECAM-1 (red), and F-actin (cyan) in Fig. 3A. In unstimulated controls, endothelial sprouts appeared short and randomly oriented, whereas dynamic strain at 5% and 15% (1 Hz) showed more elongated sprouts projecting outward from the parent vessel wall. These qualitative observations suggest the specificity of dynamic mechanical cues in guiding vascular organization and promoting angiogenic morphogenesis. To quantify changes in angiogenic sprouting architecture under different mechanical stimulation conditions, we compared three distinct parameters: total sprouting length, maximum individual sprout length, and sprout number across experimental conditions. Mechanical stimulation, independent of strain magnitude or whether the loading was static or dynamic, resulted in a substantial increase in total sprouting length compared with unstimulated controls (Fig. 3B). Further analysis of individual sprout morphology showed that the longest sprouts formed specifically under 15% dynamic (1 Hz) strain, indicating that higher dynamic strain preferentially promotes elongation of sprouts (Fig. 3C). In contrast, the 5% dynamic (1 Hz) condition yielded the highest number and density of sprouts, demonstrating that lower amplitude dynamic strain most effectively drives sprout initiation (Fig. 3D). These results collectively demonstrate that, although all forms of mechanical stimulation we tested enhanced angiogenesis, the specific strain regimen dictates whether increases in vessel formation are driven by more frequent sprouting or by elongation of individual sprouts, underscoring the role of mechanical cues in modulating vascular morphogenesis. Given that dynamic stimulation yielded more pronounced angiogenic outcomes, including evidence of lumen-like structures (Movie S4), we focused subsequent analyses on dynamic loading to investigate this response.

To examine whether mechanical strain biases angiogenic growth along its applied axis, we analyzed spatial differences in sprouting across the left–right (x-axis, along the direction of applied strain) and top–bottom (z-axis, orthogonal to the direction of applied strain) regions of the engineered vessel. Confocal z-stacks were reconstructed in 3D using Imaris imaging software, and a filament tracing algorithm was applied to segment individual sprouts and extract their spatial coordinates. Each sprout was assigned to a spatial quadrant (left, right, top, or bottom) by dividing the vessel cross-section into four regions using angular boundaries at 45°, 135°, 225°, and 315°. In unstimulated controls, sprouting was relatively isotropic across all quadrants, with no significant differences between left–right and top–bottom regions ($p > 0.05$) (Fig. 3E). When strain was applied along the x-axis, sprouting became directionally biased, with greater vessel growth observed in the left and right regions (highlighted in blue). At 5% 1Hz strain, sprouting along the strain axis increased 3.0-fold relative to unstimulated controls and 3.1-fold relative to the orthogonal axis ($p < 0.0001$). At 15% 1Hz strain, sprouting increased 2.4-fold relative to controls and 3.9-fold relative to the orthogonal axis ($p < 0.0001$). These quadrant-based differences reflect how strain magnitude influences the density of sprout initiation along the applied axis. Polar plots of representative samples further highlighted that control vessels exhibited short, evenly distributed sprouts, whereas 5% strain increased sprouting density along the x-axis, and 15% strain led to the formation of longer sprouts along the x-axis (Fig. 3F). These findings demonstrate that strain magnitude and direction modulate both the spatial patterning and length of angiogenic sprouts.

4D spatiotemporal stimulation reprograms the direction of angiogenesis

Building on our ability to pattern microvascular growth along a single axis, we next explored whether dynamically reorienting the direction of mechanical stimulation over time could reprogram sprouting trajectories in 4D (3D space and time). Using our 3-axis actuator, we applied 15% strain at 1Hz along the x-axis for the first 3 days of stimulation, followed by reorientation of the strain direction to either the y- or z-axis for the subsequent 3 days. We refer to these conditions as XX stimulation (x-axis strain maintained throughout), XY stimulation (x- followed by y-axis strain), and XZ stimulation (x- followed by z-axis strain), respectively. To assess how these directional changes influenced sprouting behavior, we visualized sprouting morphology using 3D reconstructed z-stacks, capturing both top-down and cross-sectional views of the engineered vessels. Top-down images indicate that XY stimulation induced deflection of sprouts along the y-direction (green arrows), often forming L-

shaped sprouts, in contrast to the primarily unidirectional sprouts observed under XX strain (Fig. 4A). Cross-sectional images indicate that XZ stimulation resulted in upward sprout extension along the z-axis (blue arrows), which was not observed in XX conditions (Fig. 4B).

We next quantified how the direction of strain in our 4D stimulation platform affects sprouting geometry by comparing XY and XZ conditions to XX stimulation using Imaris imaging software. To assess the effects of XY stimulation, we calculated the angle between parent and daughter branches, representing how much a sprout deviates from its original growth direction; in this analysis, the initial sprout from the parent vessel serves as the reference, and only subsequent branching events are measured. Angles closer to 0° indicate growth along the x-axis, while angles near 90° represent perpendicular branching along the y-axis (Fig. 4C). Under XX stimulation, branch angles followed a bimodal distribution with a dominant peak at 2.5° and a secondary peak at 92.5°, consistent with predominantly x-direction sprouting. In contrast, XY produced a significantly different distribution of branch angles ($p=0.018$, Kolmogorov-Smirnov test), with a unimodal peak centered at 107.5°, indicating directional reprogramming of sprout trajectories in response to y-axis strain. We also measured the absolute change in y-position ($|\Delta y|$) for each sprout and found a 1.3-fold increase in XY versus XX conditions ($p = 0.0007$), further confirming sprout deflection along the y-axis (Fig. 4D)**.** To quantify the effects of XZ stimulation, we extracted the absolute change in z-position ($|\Delta z|$) for each sprout (Fig. 4E). Compared to XX stimulation, XZ stimulation resulted in a 1.7-fold increase in z-axis displacement ($p=0.0127$), demonstrating directional reprogramming of sprout trajectories in response to z-axis strain.

Permeability measurements revealed no significant differences among the multi-directionally stimulated groups (XX, XY, XZ; $p>0.05$) (Fig. 4F), suggesting that 3D directional reprogramming of angiogenesis can occur without compromising barrier integrity. Altogether, these results demonstrate that dynamic, multi-axial 4D mechanical stimulation can be used to precisely direct and redirect sprouting trajectories across all three spatial dimensions while maintaining vascular barrier function.

RNA sequencing identifies transcriptional changes associated with mechanically stimulated angiogenesis

Given the distinct morphological and functional changes observed under mechanical stimulation, we investigated the molecular mechanisms underlying these strain-induced behaviors. Since cell-ECM interactions can strongly influence endothelial behavior, we first examined whether mechanical actuation altered the collagen hydrogel's fibrillar architecture. Collagen fibers were visualized using the Rhobo6 fluorescent ECM-binding probe (36), and fiber orientation was quantified in the region between the magnetic actuator and the vessel. No significant differences ($p = 0.55$) in collagen fiber orientation were observed between unstimulated (0% strain) and dynamically actuated (15% 1Hz) conditions (Fig. 5A). These results indicated that dynamic magnetic matrix actuation did not significantly alter ECM microstructure, suggesting that observed endothelial responses could not be attributed to matrix remodeling.

We thus performed bulk RNA sequencing (RNA-seq) to compare gene expression between the unstimulated control, 5% 1Hz and 15% 1Hz strain conditions. Principal component analysis revealed clear separation between stimulated and control samples, while 5% 1Hz and 15% 1Hz strain conditions clustered closely together (Fig. 5B). Volcano plots for the pairwise comparisons highlighted up-regulated (red) and down-regulated (blue) differentially expressed genes (DEGs) (p. adjust < 0.05, $|\log_2 \text{fold change}| > 0.7$) (Fig. 5C). Differential expression analysis identified 570 DEGs under 15% 1Hz strain and 504 DEGs under 5% 1Hz strain, with 387 genes (56.4%) shared between both groups (Fig. 5D). Hierarchical clustering of Hallmark angiogenesis genes further showed that both strain conditions clustered together and were distinct from the unstimulated control, with upregulation of pro-angiogenic genes including *VEGFA, FGFR1, PTK2,* and *PDGFA* (Fig. 5E) (37).

Gene set enrichment analysis (GSEA) was then used to interpret the functional significance of these transcriptional changes. Across both mechanically stimulated conditions, pathways associated with angiogenesis and cytoskeletal regulation exhibited positive normalized enrichment scores (NES > 1), including regulation of cell-substrate adhesion, cell migration in sprouting angiogenesis, endothelial cell proliferation, and regulation of cell shape, whereas pathways related to vascular permeability, apoptosis, and blood vessel regression showed negative enrichment (NES < 1) (Fig. 5F).

To further identify specific mechanosensitive mediators of this response, we explored a subset of genes with established roles in mechanosensing, transcriptional regulation, ECM remodeling, and barrier stabilization (Fig. S3A). Among the mechanosensors, the stretch-inducible adaptor *ANKRD1* was significantly upregulated under 15% strain ($p_{adj} < 0.05$), consistent with its known roles in endothelial migration, survival, and neovascularization during tissue repair (38). The focal adhesion gene *ZYX* was strongly expressed under both 5% and 15% strain ($p_{adj} < 0.001$), and has been shown to transduce mechanical signals to the nucleus in endothelial cells and regulate stretch-sensitive gene expression (39, 40). Within sprouting-associated transcriptional regulators, *FOSB* was significantly upregulated in both 5% and 15% strain conditions ($p_{adj} < 0.05$ and < 0.01, respectively). As a mechanosensitive AP-1 family transcription factor, *FOSB* is upregulated by cyclic stretch in endothelial cells and contributes to AP-1 complexes that regulate endothelial genes involved in angiogenesis and vascular remodeling (40, 41). The ECM and migration group showed robust gene upregulation across both strain magnitudes, with *ABI3BP*, *SPOCK1*, *COL8A1*, and *CTTN* all significantly upregulated ($p_{adj} < 0.001$) relative to control, suggesting enhanced substrate engagement and focal-adhesion remodeling that could facilitate sprouting behavior (42–45). In particular, *CTTN*, which localizes to adherens junctions and links actin dynamics to barrier regulation, may further contribute to strain-induced strengthening of endothelial junctions (44, 46). Supporting this, the upregulation of *SERPINE2* and downregulation of *P2RY1* align with our functional findings of strengthened barrier integrity under strain, consistent with transcriptional patterns that may support junctional stability while enabling controlled endothelial remodeling (47, 48). Together, these results may provide insight into a coordinated endothelial transcriptional program that integrates mechanosensing, angiogenic activation, and barrier stabilization under dynamic mechanical strain.

Discussion

Angiogenesis occurs in mechanically dynamic environments where tissue deformation, blood flow-induced stretch, and interstitial pressure continuously remodel the vasculature (19). While previous studies have identified mechanical forces as regulators of endothelial behavior (14, 49, 50), systematic investigation of how strain magnitude, frequency, spatial patterning, and temporal patterning modulate 3D angiogenic sprouting and barrier function has been limited. Previous studies have shown that cyclic mechanical strain influences endothelial cell morphology and orientation (20, 51), Yet, how the temporal dynamics of mechanical stimulation, distinct strain magnitudes, and distinct strain directions collectively influence directional angiogenic sprouting and microvascular network architecture in 3D tissue models remained poorly understood. In our study, strain magnitudes of 5–15% were chosen to match the physiological range of tensile loading experienced by blood vessels embedded in native extracellular matrices.(20) Furthermore, dynamic stimulation at 1 Hz was employed to recreate the oscillatory mechanical environment characteristic of living tissue ECMs, critical for blood vessel remodeling.(52)

Our systematic analysis revealed that dynamic mechanical stimulation, regardless of strain magnitude (5% or 15%) or temporal pattern (static or 1 Hz), reduced permeability to 10- and 40-kDa dextran tracers by approximately 2-fold and 1.5-fold, respectively. These results suggest that physiological strain engages a threshold-dependent mechanotransduction mechanism that enhances barrier integrity through actin cytoskeletal reorganization (53–55). In contrast to 2D systems where uniaxial strain drives perpendicular alignment (56), endothelial cells in our 3D

vessels experience circumferential loading that promotes longitudinal junction organization. Sprouting endothelium thus interprets strain direction as a guidance cue, not a stabilizing signal, as supported by increased expression of *ABI3BP, SPOCK1, COL8A1,* and *CTTN*. Notably, our analysis of endothelial junction orientation was based on z-projections of the parent vessel, which may not fully capture organization at the vessel-gel interface where sprouting occurs, motivating future studies that examine cells at this interface to provide additional insights into junctional remodeling under mechanical stimulation.

In contrast to the magnitude-independent barrier response, sprouting morphology exhibited pronounced sensitivity to strain magnitude. While all mechanical stimulation increased total sprouting length, 5% dynamic strain maximized sprout number (density), whereas 15% dynamic strain produced the longest individual sprouts. This two-mode angiogenic response is consistent with previous work showing that moderate strain activates vessel formation pathways, whereas higher strain shifts the response toward MMP-driven matrix remodeling. (16) The shared upregulation of ECM remodeling genes (*ABI3BP, SPOCK1, COL8A1, CTTN*) across both 5% and 15% conditions indicates a common pro-angiogenic transcriptional program activated by dynamic mechanical stimulation. Notably, sprouts in all stimulated conditions were observed to have hollow capillary-scale architectures (< 10 μm) that cannot readily be patterned using alternative fabrication approaches such as 3D bioprinting, highlighting our ability to leverage dynamic forces to pattern organized microvascular networks.

Leveraging quantitative mapping of sprouting trajectories in 3D, our results further demonstrate that mechanical strain provides a spatially instructive cue that biases angiogenic sprouting along the axis of deformation. When applied dynamically, unidirectional strain induced a significant increase in sprouting along the strain axis, with 3.0-fold and 2.4-fold increases in sprout number for 5% and 15% conditions, respectively, relative to unstimulated controls. A unique contribution of our study is demonstrating how dynamically changing the axis of stimulation reprograms sprouting trajectories over time. Sequential application of strain along different axes, including y-and z-axis loading, produced L-shaped sprouts and deflection along the y- or z-direction, indicating that endothelial cells continuously adapt to evolving mechanical environments rather than adhering to a predetermined growth program. While previous studies have shown that the direction of static stretch or flow can influence sprouting orientation (57–59), the ability to temporally redirect angiogenic sprouting has not been demonstrated in previous angiogenesis models, to our knowledge. The ability to steer 3D sprouting through controlled multi-directional strain, without measurable changes in permeability across x-, y-, and z-stimulated conditions, indicates continuous mechanosensing through focal adhesion components such as *ZYX* and dynamic actin remodeling mediated by *CTTN* (39, 44, 46).

To uncover the molecular basis of mechanically regulated angiogenesis, we performed transcriptomic profiling of endothelialized vessels subjected to dynamic strain. Bulk RNA sequencing revealed transcriptional remodeling in response to both 5% and 15% strain, with 387 DEGs (56.4% overlap) shared between the two conditions. We observed minimal transcriptional divergence between 5% and 15% strain conditions, potentially because both magnitudes fall within a physiological range sufficient to activate a common mechanotransduction program. GSEA revealed robust enrichment of pathways associated with cell-substrate adhesion, cell migration in sprouting angiogenesis, endothelial cell proliferation, and regulation of cell shape, while pathways related to vascular permeability, apoptosis, and vessel regression were suppressed. This transcriptional signature aligns with our functional observations of enhanced sprouting and strengthened barrier function. Upregulation of *VEGFA, FGFR1, PTK2 (FAK),* and *PDGFA* confirms activation of canonical pro-angiogenic signaling, consistent with previous studies showing that cyclic tensile strain triggers autocrine Ang-2 and paracrine PDGF-ββ signaling to enhance endothelial sprouting (22). To our knowledge, this is the first study to investigate how varying strain magnitudes modulate endothelial gene expression in a 3D vascular system.

Our study provides important insights into mechanically regulated angiogenesis; however, several limitations should be considered when interpreting our findings. Our human vessel-on-chip platform currently includes only endothelial cells, motivating future iterations of our platform that integrate smooth muscle cells, pericytes, and fibroblasts to better mimic the cellular and structural complexity characteristic of native vasculature (60). In this work, we primarily focused on physiological strain magnitudes (5–15%) and a frequency of 1 Hz, relevant to oscillatory ECM environments of mechanically active tissues (e.g. heart, lungs, and muscle) (61). The response to pathological strains (>20%) or higher-frequency stimulation (>2 Hz) occurring in trauma or disease states thus remains unexplored (62, 63). Additionally, we conducted all experiments under static media culture conditions without incorporating physiological perfusion to isolate the effects of matrix-applied strain from confounding flow-derived forces such as shear stress. While it has been shown that flow contributes to the regulation of cell–cell junction organization, permeability, and angiogenic gene expression (64), decoupling these variables allowed us to specifically examine the influence of strain on angiogenic behavior. Although cyclic deformation at 1 Hz may generate transient flow with minimal, periodic shear within vessels, we observed no induction of shear-responsive genes (*KLF2, eNOS*) (56), whereas mechanical stimulation upregulated ECM/migration genes (*SPOCK1, COL8A1, CTTN*) and mechanosensitive markers (*ZYX, ANKRD1*), consistent with strain-driven rather than flow-driven signaling. We also acknowledge that in the absence of continuous flow, periodic media changes may have led to transient nutrient or oxygen gradients, which may influence the local microenvironment and contribute to depth-dependent sprouting behavior.

We observed that collagen fiber architecture remained unchanged across all mechanical conditions in our system, in contrast to other studies reporting mechanical remodeling of ECM fibers under strain (65). This is consistent with our prior work using magnetic matrix actuation platforms, where fibrin-based matrices also showed no reorganization under dynamic strain (32), suggesting that not all ECM materials undergo mechanically induced remodeling. Furthermore, given the lack of fibroblast-derived MMP activity in our endothelial-only model (66), the cellular and transcriptional changes observed cannot be attributed to matrix remodeling. While our RNA-seq revealed high transcriptional overlap between 5% and 15% strain conditions, the specific mechanisms by which strain magnitude differentially shapes sprouting phenotypes require further investigation. Future loss-of-function studies targeting candidate mechanosensors could potentially uncover the signaling pathways responsible for magnitude-specific sprouting responses. Single-cell and spatial transcriptomic approaches may also reveal endothelial subpopulation heterogeneity in mechanical sensing and how these responses are spatially organized within the 3D environment.

In conclusion, our findings demonstrate that mechanical forces regulate angiogenesis through coordinated effects of strain magnitude, frequency, and 4D spatiotemporal patterning. Dynamic strain at physiological magnitudes enhances endothelial alignment, sprouting, and barrier function through activation of mechanosensors, transcription factors, and ECM remodeling genes, with strain magnitude influencing whether angiogenic responses favor sprout initiation (5%) or elongation (15%). Despite substantial changes in vascular morphology, barrier function remained intact across all mechanical stimulation conditions, underscoring the potential of multi-axial actuation to engineer spatially organized yet functionally robust vascular networks. Notably, our study is the first to demonstrate that sequential, multi-directional mechanical stimulation can reprogram angiogenic trajectories over time, enabling dynamic control of sprouting geometry across all three spatial dimensions. These results build upon previous work in 2D and uniaxial systems by extending the concept of strain-guided angiogenesis into a fully 3D microenvironment with programmable mechanical inputs. Together, these insights have important implications for regenerative medicine and disease modeling, where precisely patterned dynamic mechanical cues could be harnessed to guide vascular morphogenesis in engineered tissues and organoids and to modulate pathological angiogenesis in cancer, retinopathy, and ischemia.

Materials and Methods

Device fabrication
The culture chamber was assembled from four polymethyl methacrylate (PMMA) side plates (⅛ inch thickness, McMaster Carr) using an acrylic adhesive (Weld-On 4). The two end wall plates have a 650μm diameter hole. All PMMA pieces were cut using a CO2 laser (Laser Cutter Epilog Fusion 40). The culture chamber was then bonded to a square glass coverslip (No. 2 glass, VWR) using double-sided adhesive tape (9474LE, 3M)(67). The internal length, width, and depth were 10mm, 4mm, and 3.175mm, respectively (Fig. S1A-B). The devices were then autoclaved for sterilization. Magnetic actuators were cut from commercial neodymium magnet sheets (thickness: 16 mil, Bandle B) using an electronic cutting plotter (Silhouette Cameo 4, Silhouette America).

Cell culture and seeding in the microfluidic device
ImHUVECs expressing blue fluorescent protein (BFP, passages 12–20) were cultured in VascuLife VEGF-Mv Endothelial medium (Lifeline Cell Technology), with medium changes every 2 days. Cells were detached with TrypLE Express (Gibco) upon reaching ~80% confluency and seeded into microfluidic devices.

The fabrication process of the vascular construct is shown in Figure S1. Briefly, a single glass rod (DWK Life Sciences) was inserted into the central channel of the device. Next, 180 μL of collagen solution (2.4 mg/mL, porcine tendon, Cellmatrix Type I-A) was prepared on ice and cast into the device. A BSA-treated 3D-printed stamp was then aligned with the device using the built-in features to create a void space for the magnetic actuator. The device was incubated for 1h at 37 ºC for collagen gelation. Next, the stamp was carefully removed from the device, and the magnetic actuator was positioned in the patterned void space, followed by the addition of 80 μL premixed collagen to sandwich the actuator. This top collagen layer was gelled at 37 °C for 1 h. The glass rod was then removed, and any residual liquid in the channel was aspirated with a pipette to yield a hollow lumen. A 10 μL suspension of ImHUVECs (8×10^6 cells/mL) was injected into the lumen, and devices were incubated at 37 °C for 2 h on a Tube Revolver Rotator platform (Thermo Scientific) to promote uniform 3D lining of the channel. Each device was maintained in a 6-well plate (VWR) with 5 mL of culture medium to fully submerge the construct, and the medium was replenished every 2 days.

Strain characterization and high-throughput mechanical stimulation
Green fluorescent polystyrene microspheres (Fisher Scientific) were embedded within the hydrogel to track matrix deformation. Videos were recorded using an EVOS fluorescence microscope and processed using the authors' previously developed open-source computational framework (https://github.com/HibaKob/Raman_Manuscript_2023)(31) to calculate the subdomain-averaged strain in each row over time.

High-throughput automated stimulation setup
A custom-built high-throughput stimulation platform was developed by repurposing a benchtop three-axis linear actuator system originally designed for computer numerical control (CNC) milling (3020-PRO MAX V2, Genmitsu). The base assembly included motorized X, Y, and Z linear actuators that provided programmable motion in all three dimensions (motion range: X 300mm; Y 205 mm; Z 78 mm; positional accuracy ±0.1 mm). To adapt the system for magnetic stimulation experiments, a custom 3D-printed holder was designed and mounted onto the actuator arm to secure an array of up to nine external neodymium magnets (3896.66 Surface Gauss, 0.750" L x 0.375" W x 0.375" H, Radial Magnets) above the vessel-on-a-chip devices. A 3D-printed well plate insert was fabricated to position the chips precisely within standard 6-well plates. A multi-well plate holder was also added to the stage to accommodate up to three well plates simultaneously, enabling parallel mechanical stimulation experiments. The entire system was controlled via G-code instructions, providing programmable control over magnet motion parameters, including direction, distance, and frequency of actuation. The automated setup was housed within a standard

laboratory oven maintained at 37°C to ensure physiological conditions throughout the stimulation period.

Permeability measurement

To assess vascular barrier permeability, devices were perfused with fluorescent dextran (10 kDa Texas Red and 40 kDa Alexa Fluor 647, Invitrogen) on day 7. Permeability measurements were performed specifically on straight segments of the parent vessel, with regions of interest (ROIs) defined based on dextran fluorescence within the vessel wall, which did not include angiogenic sprout regions. Dextran diffusion from the parent vessel into the ECM was imaged in real-time using the Nikon AXR confocal microscope. Confocal z-stacks were acquired every 2 minutes over 10 minutes (10 kDa) and 30 minutes (40 kDa), and maximum intensity projection images were used for analysis. The diffusive permeability coefficient (P_D) was calculated in MATALB by analyzing the changes in fluorescence intensity in the vessel and ECM. The diffusion profile was fitted to a dynamic mass-conservation equation $J = P_D (c_{vessel} - c_{ECM})$, where J is the mass flux of dextran, c_{vessel} dextran concentration in the parent vessel, and c_{ECM} is the dextran concentration in the surrounding ECM, following established methods(34, 35).

Immunofluorescence staining and microscopy

To visualize endothelial sprouting, the cells in the devices were fixed with 4% paraformaldehyde for 20 minutes at room temperature, permeabilized with 0.2% Triton X-100/PBS for 5 minutes, and blocked in 1% BSA in 0.2% Triton X-100/PBS for 30 minutes. The cells were then washed three times with 0.2% Triton X-100/PBS for 5 minutes each and incubated overnight at 4°C with Alexa Fluor 488-conjugated mouse anti-human platelet/endothelial cell adhesion molecule-1 (PECAM-1, 1:300 dilution, Cell Signaling Technology). After overnight incubation, the cells were rinsed three times with 0.2% Triton X-100/PBS and incubated with Alexa Fluor Plus 555 Phalloidin (1:400 dilution, Thermo Fisher Scientific) for 20 minutes at room temperature. The cells were then washed three times with PBS and stored in PBS for immunofluorescence imaging. Fluorescence images were captured on a Nikon AXR point scanning confocal microscope using 4x, 10x, and 20x objectives (Nikon) and processed using the Nikon Denoise.ai software and ImageJ.

Sprouting quantification

Sprouting was quantified from confocal images of cells immunostained for F-actin. For each device, maximum projection images of the full vessel were thresholded to isolate vascular structures, despeckled to remove noise, and skeletonized. The skeletonized images were then analyzed using a custom graph-based algorithm implemented in Wolfram Mathematica. Each binary skeleton was converted to a morphological graph, where continuous vessel and sprout segments were represented as edges, and branch junctions (vertices with degree >2) and terminal sprout tips (vertices with degree=1) were represented as vertices.

The graph was decomposed into connected components relative to primary branch points, corresponding to the origins of sprouts from the parent vessel. For each connected component, sprouting metrics were calculated by selecting the parent branch point and computing Euclidean distances to all associated endpoints. The maximum sprout length was defined as the longest Euclidean distance from the parent vessel to a terminal endpoint, and the total sprout length as the sum of all distances within the component.

To analyze daily changes in sprouting, images of the BFP-tagged nuclei signal across the full vessel were acquired. Maximum projection images were processed in Fiji using the Huang thresholding method to generate binary vessel masks. Since the BFP signal does not form a continuous structure suitable for skeletonization, the perimeters of the masks were extracted using the Analyze Particles function to determine the vessel boundary contour length, which served as a global metric of sprouting across the full vessel. For each device, contour lengths from each day were normalized to the value measured on the day stimulation began.

Orientation analysis
The orientation of endothelial cells within the vascular constructs was quantified using immunostaining for PECAM-1, a marker of cell–cell junctions. The entire constructs were imaged using a Nikon AXR confocal microscope, and Z-stack images were acquired across the full height of the vessels. Maximum intensity projections of the Z-stacks were generated for analysis. ImageJ (NIH) with the OrientationJ plugin was used to measure the angular distribution of endothelial cells under different experimental conditions. (68) The resulting images were displayed in HSB color, where hue indicates orientation, saturation represents coherency, and brightness corresponds to the original signal intensity.

Collagen fibers were stained with Rhobo-6 (36) and imaged using confocal imaging. Fiber orientation was quantified using an identical OrientationJ workflow, and differences in alignment were compared across the various mechanical stimulation conditions.

Image analysis and 3D vessel reconstruction
Confocal microscopy images of immunofluorescently labeled vascular networks were acquired using the Nikon AXR confocal microscope. Image stacks were processed using Imaris image analysis software (Oxford Instruments, version 10.1). 3D reconstructions of the vascular structures were generated from the complete z-stacks to capture the full morphology and spatial organization of sprouting angiogenesis within the tissue constructs. The coordinates of all filament skeleton nodes were extracted using the "Filament Point Tracking" module, a MATLAB-integrated feature within Imaris, which exports the complete set of (x, y, z) coordinates for every segment. These coordinates were then used for downstream spatial analyses, including quantification of sprout positions and their growth directions. The Angle Measurement tool within Imaris was also employed to compute the angles between sprouts at branch points, providing quantitative information on the three-dimensional organization and branching orientation of sprouts. All quantitative data generated using the Imaris Filament Tracer, Filament Point Tracking, and Angle Measurement modules were exported as CSV files and subsequently processed and analyzed using MATLAB (MathWorks) and GraphPad Prism 10 to perform statistical analysis and generate graphical representations.

RNA extraction, sequencing, and analysis
Cells were extracted by removing the gel from the devices and digesting each gel in 500 µL of 0.5 mg/mL Liberase TM (Sigma Aldrich) in VascuLife Basal Medium for 20 minutes at 37°C on a revolver(69). Cells were pooled from 2 devices. RNA extraction was performed on the isolated cells using a RNeasy Mini Kit (Qiagen) following the manufacturer instructions. Bulk RNA sequencing was performed by the MIT BioMicro Center. Sequencing libraries were generated using the Low Input hs|mm ZapR protocol with rRNA depletion and strand-specific preparation, followed by quality assessment. Libraries were sequenced on a Singular G4 platform with 50 bp paired-end reads.

Raw FASTQ files were processed using the nf-core/rnaseq pipeline (v3.17.0). Transcript abundances were quantified using Salmon with the GENCODE v47 human transcriptome as reference. Differential expression analysis was performed in DESeq2 (v1.42.1) with log2 fold-change shrinkage via the apeglm method, and statistical significance was determined using the Benjamini–Hochberg false discovery rate (FDR ≤ 0.05). Functional enrichment was performed with fgsea using MSigDB Hallmark and C5 Gene Ontology Biological process collections, and results were visualized in R (v4.3) using ggplot2 and ComplexHeatmap.

Statistical analysis
All error bars are shown as mean ± standard deviation, and sample sizes are reported in figure legends. Statistical analysis was performed using GraphPad Prism 10. Ordinary one-way or two-way ANOVA with Tukey's multiple comparisons test was applied to analyses involving more than

two groups, and two-tailed unpaired t-tests were applied to analyses involving two groups. * indicates $p<0.05$, ** indicates $p<0.01$, *** indicates $p<0.001$, **** indicates $p<0.0001$, and ns indicates $p>0.05$.

Acknowledgments

This work was supported by a DoD Army Research Office Early Career Program and PECASE grant (W911NF-22-1-0126, awarded to R.R.) and a DoD DURIP Program grant (W911NF-24-1-0106, awarded to R.R.). S.K. acknowledges support from the Natural Sciences and Engineering Research Council of Canada (NSERC) Postdoctoral Fellowship, and J.S. acknowledges support from the National Science Foundation Graduate Research Fellowship Program (NSF-GRFP). We thank Dr. Kayvon Pedram for assistance with Rhobo6 imaging and Dr. Zhengpeng (Jason) Wan for providing the cell line. We acknowledge the RNA sequencing support provided by the MIT BioMicro Center and imaging support from the Koch Institute Microscopy Core Facility. We also thank Sonika Kohli and Vesper Evereux for their assistance with device fabrication.

References

1. S. Fleischer, D. N. Tavakol, G. Vunjak-Novakovic, From arteries to capillaries: approaches to engineering human vasculature. *Adv. Funct. Mater.* **30**, 1910811 (2020).
2. N. Zhao, A. F. Pessell, N. Zhu, P. C. Searson, Tissue-Engineered Microvessels: A Review of Current Engineering Strategies and Applications. *Adv. Healthc. Mater.* **13**, 2303419 (2024).
3. T. Rademakers, J. M. Horvath, C. A. van Blitterswijk, V. L. S. LaPointe, Oxygen and nutrient delivery in tissue engineering: Approaches to graft vascularization. *J. Tissue Eng. Regen. Med.* **13**, 1815–1829 (2019).
4. R. H. Heisser, M. Bawa, J. Shah, A. Bu, R. Raman, Soft Biological Actuators for Meter-Scale Homeostatic Biohybrid Robots. *Chem. Rev.* **125**, 3976–4007 (2025).
5. R. Z. Zhuang, F. Chesnais, G. Vunjak-Novakovic, Integrating Hierarchical Vasculature into Engineered Cardiac Tissues. *Adv. Mater.* **n/a**, e09242.
6. Y. Wang, M. Keshavarz, P. Barhouse, Q. Smith, Strategies for Regenerative Vascular Tissue Engineering. *Adv. Biol.* **7**, 2200050 (2023).
7. S. Landau, *et al.*, Bioengineering vascularization. *Development* **151**, dev204455 (2024).
8. O. Aydin, *et al.*, Principles for the design of multicellular engineered living systems. *APL Bioeng.* **6**, 010903 (2022).
9. D. B. Kolesky, K. A. Homan, M. A. Skylar-Scott, J. A. Lewis, Three-dimensional bioprinting of thick vascularized tissues. *Proc. Natl. Acad. Sci.* **113**, 3179–84 (2016).
10. P. Carmeliet, R. K. Jain, Molecular mechanisms and clinical applications of angiogenesis. *Nature* **473**, 298–307 (2011).
11. N. Walji, S. Kheiri, E. W. K. Young, Angiogenic Sprouting Dynamics Mediated by Endothelial-Fibroblast Interactions in Microfluidic Systems. *Adv. Biol.* **5**, 2101080 (2021).
12. D. Rana, *et al.*, Bioprinting of Aptamer-Based Programmable Bioinks to Modulate Multiscale Microvascular Morphogenesis in 4D. *Adv. Healthc. Mater.* **14**, 2402302 (2025).
13. F. E. Freeman, *et al.*, 3D bioprinting spatiotemporally defined patterns of growth factors to tightly control tissue regeneration. *Sci. Adv.* **6**, eabb5093 (2020).
14. J. Flournoy, S. Ashkanani, Y. Chen, Mechanical regulation of signal transduction in angiogenesis. *Front. Cell Dev. Biol.* **10** (2022).
15. E. A. Silva, D. J. Mooney, Effects of VEGF temporal and spatial presentation on angiogenesis. *Biomaterials* **31**, 1235–1241 (2010).
16. N. F. Jufri, A. Mohamedali, A. Avolio, M. S. Baker, Mechanical stretch: physiological and pathological implications for human vascular endothelial cells. *Vasc. Cell* **7**, 8 (2015).

17. N. V. Bukoreshtliev, K. Haase, A. E. Pelling, Mechanical cues in cellular signalling and communication. *Cell Tissue Res.* **352**, 77–94 (2013).
18. Q. Smith, *et al.*, Cytoskeletal tension regulates mesodermal spatial organization and subsequent vascular fate. *Proc. Natl. Acad. Sci.* **115**, 8167–8172 (2018).
19. X. R. Lim, O. F. Harraz, Mechanosensing by Vascular Endothelium. *Annu. Rev. Physiol.* **86**, 71–97 (2024).
20. S. Barrasa-Ramos, C. A. Dessalles, M. Hautefeuille, A. I. Barakat, Mechanical regulation of the early stages of angiogenesis. *J. R. Soc. Interface* **19**, 20220360 (2022).
21. T. Korff, H. G. Augustin, Tensional forces in fibrillar extracellular matrices control directional capillary sprouting. *J. Cell Sci.* **112**, 3249–3258 (1999).
22. D. Rosenfeld, *et al.*, Morphogenesis of 3D vascular networks is regulated by tensile forces. *Proc. Natl. Acad. Sci.* **113**, 3215–3220 (2016).
23. R. Kaunas, S. Usami, S. Chien, Regulation of stretch-induced JNK activation by stress fiber orientation. *Cell. Signal.* **18**, 1924–1931 (2006).
24. J. H.-C. Wang, P. Goldschmidt-Clermont, J. Wille, F. C.-P. Yin, Specificity of endothelial cell reorientation in response to cyclic mechanical stretching. *J. Biomech.* **34**, 1563–1572 (2001).
25. D. Ferrari, *et al.*, Effects of biomechanical and biochemical stimuli on angio- and vasculogenesis in a complex microvasculature-on-chip. *iScience* **26**, 106198 (2023).
26. A. Shimizu, *et al.*, ECM-based microchannel for culturing in vitro vascular tissues with simultaneous perfusion and stretch. *Lab. Chip* **20**, 1917–1927 (2020).
27. L. Debbi, *et al.*, The Effect of Mechanical Loading on Sprouting Angiogenesis from Engineered Macro-vessel Model. *Small Methods* **n/a**, e00850 (2025).
28. E. Gonzalez-Saiz, M. L. Lopez-Donaire, L. Gutiérrez, K. Danas, D. Garcia-Gonzalez, Magnetic-Driven Viscous Mechanisms in Ultra-Soft Magnetorheological Elastomers Offer History-Dependent Actuation with Reprogrammability Options. *Adv. Sci.* **12**, e06790 (2025).
29. M. A. Moreno-Mateos, *et al.*, Magneto-mechanical system to reproduce and quantify complex strain patterns in biological materials. *Appl. Mater. Today* **27**, 101437 (2022).
30. D. Garcia-Gonzalez, R. Raman, S. Schuerle, A. Tay, Magnetic Actuation for Mechanomedicine. *Adv. Intell. Syst.* **7**, 2400638 (2025).
31. B. Rios, *et al.*, Mechanically programming anisotropy in engineered muscle with actuating extracellular matrices. *Device* **1** (2023).
32. A. Bu, *et al.*, Actuating Extracellular Matrices Decouple the Mechanical and Biochemical Effects of Muscle Contraction on Motor Neurons. *Adv. Healthc. Mater.* **14**, 2403712 (2025).
33. C. O'Connor, E. Brady, Y. Zheng, E. Moore, K. R. Stevens, Engineering the multiscale complexity of vascular networks. *Nat. Rev. Mater.* **7**, 702–716 (2022).
34. W. J. Polacheck, M. L. Kutys, J. B. Tefft, C. S. Chen, Microfabricated blood vessels for modeling the vascular transport barrier. *Nat. Protoc.* **14**, 1425–1454 (2019).
35. W. J. Polacheck, *et al.*, A non-canonical Notch complex regulates adherens junctions and vascular barrier function. *Nature* **552**, 258–262 (2017).
36. A. Fiore, *et al.*, Live imaging of the extracellular matrix with a glycan-binding fluorophore. *Nat. Methods* 1–11 (2025). https://doi.org/10.1038/s41592-024-02590-2.
37. A. Liberzon, *et al.*, The Molecular Signatures Database Hallmark Gene Set Collection. *Cell Syst.* **1**, 417–425 (2015).
38. X. Xu, *et al.*, Research progress of ankyrin repeat domain 1 protein: an updated review. *Cell. Mol. Biol. Lett.* **29**, 131 (2024).
39. A. Wójtowicz, *et al.*, Zyxin Mediation of Stretch-Induced Gene Expression in Human Endothelial Cells. *Circ. Res.* **107**, 898–902 (2010).
40. Y. Fang, D. Wu, K. G. Birukov, Mechanosensing and Mechanoregulation of Endothelial Cell Functions. *Compr. Physiol.* **9**, 873–904 (2019).
41. B. E. Sumpio, W. Du, W.-J. Xu, Exposure of Endothelial Cells to Cyclic Strain Induces c-fos, fosB and c-jun But not jun B or jun D and Increases the Transcription Factor AP-1. *Endothelium* **2**, 149–156 (1994).

42. Q. Li, *et al.*, COL8A1 Regulates Endothelial Phenotype in Inflammatory Endothelial-to-Mesenchymal Transition. *Am. J. Physiol.-Heart Circ. Physiol.* (2025). https://doi.org/10.1152/ajpheart.00339.2025.
43. L. Váncza, P. Tátrai, A. Reszegi, K. Baghy, I. Kovalszky, SPOCK1 with unexpected function. The start of a new career. *Am. J. Physiol.-Cell Physiol.* **322**, C688–C693 (2022).
44. S. Moztarzadeh, *et al.*, Cortactin is in a complex with VE-cadherin and is required for endothelial adherens junction stability through Rap1/Rac1 activation. *Sci. Rep.* **14**, 1218 (2024).
45. D. A. Delfín, J. L. DeAguero, E. N. McKown, The Extracellular Matrix Protein ABI3BP in Cardiovascular Health and Disease. *Front. Cardiovasc. Med.* **6** (2019).
46. X. Sun, *et al.*, Genetic and epigenetic regulation of cortactin (CTTN) by inflammatory factors and mechanical stress in human lung endothelial cells. *Biosci. Rep.* **44**, BSR20231934 (2024).
47. L. Idir, *et al.*, SerpinE2 deficiency exacerbates glomerular injury in diabetic nephropathy through dysregulated angiogenesis and inflammatory responses. *Am. J. Physiol.-Ren. Physiol.* **329**, F548–F556 (2025).
48. J. K. Hennigs, *et al.*, The P2-receptor-mediated Ca2+ signalosome of the human pulmonary endothelium - implications for pulmonary arterial hypertension. *Purinergic Signal.* **15**, 299–311 (2019).
49. S. C. R. Staples, *et al.*, Intussusceptive angiogenesis-on-a-chip: Evidence for transluminal vascular bridging by endothelial delamination. *Proc. Natl. Acad. Sci.* **122**, e2423700122 (2025).
50. A. N. Ivanov, Yu. R. Chabbarov, Mechanisms of Physiological Angiogenesis. *J. Evol. Biochem. Physiol.* **59**, 914–929 (2023).
51. I. S. Joung, M. N. Iwamoto, Y.-T. Shiu, C. T. Quam, Cyclic strain modulates tubulogenesis of endothelial cells in a 3D tissue culture model. *Microvasc. Res.* **71**, 1–11 (2006).
52. P. M. Cummins, *et al.*, Cyclic strain-mediated matrix metalloproteinase regulation within the vascular endothelium: a force to be reckoned with. *Am. J. Physiol.-Heart Circ. Physiol.* **292**, H28–H42 (2007).
53. P. Keshavanarayana, F. Spill, A mechanical modeling framework to study endothelial permeability. *Biophys. J.* **123**, 334–348 (2024).
54. Y. L. Dorland, S. Huveneers, Cell–cell junctional mechanotransduction in endothelial remodeling. *Cell. Mol. Life Sci.* **74**, 279–292 (2017).
55. A. Bancaud, *et al.*, Intraluminal pressure triggers a rapid and persistent reinforcement of endothelial barriers. *Lab. Chip* **25**, 2061–2072 (2025).
56. S. Chien, Mechanotransduction and endothelial cell homeostasis: the wisdom of the cell. *Am. J. Physiol.-Heart Circ. Physiol.* **292**, H1209–H1224 (2007).
57. S. Das, A. Ippolito, P. McGarry, V. S. Deshpande, Cell reorientation on a cyclically strained substrate. *PNAS Nexus* **1**, pgac199 (2022).
58. P. A. Galie, *et al.*, Fluid shear stress threshold regulates angiogenic sprouting. *Proc. Natl. Acad. Sci.* **111**, 7968–7973 (2014).
59. K. Haase, *et al.*, Physiologic flow-conditioning limits vascular dysfunction in engineered human capillaries.
60. H. Kim, T. Osaki, R. D. Kamm, H. H. Asada, Tri-culture of spatially organizing human skeletal muscle cells, endothelial cells, and fibroblasts enhances contractile force and vascular perfusion of skeletal muscle tissues. *FASEB J.* **36**, e22453 (2022).
61. C. A. Dessalles, C. Leclech, A. Castagnino, A. I. Barakat, Integration of substrate- and flow-derived stresses in endothelial cell mechanobiology. *Commun. Biol.* **4**, 1–15 (2021).
62. Y. Song, *et al.*, The Molecular Mechanism of Aerobic Exercise Improving Vascular Remodeling in Hypertension. *Front. Physiol.* **13** (2022).
63. I. A. Tamargo, K. I. Baek, Y. Kim, C. Park, H. Jo, Flow-induced reprogramming of endothelial cells in atherosclerosis. *Nat. Rev. Cardiol.* **20**, 738–753 (2023).
64. M. Cherubini, *et al.*, Flow in fetoplacental-like microvessels in vitro enhances perfusion, barrier function, and matrix stability. *Sci. Adv.* **9**, eadj8540 (2023).

65. M. G. McCoy, *et al.*, Collagen Fiber Orientation Regulates 3D Vascular Network Formation and Alignment. *ACS Biomater. Sci. Eng.* **4**, 2967–2976 (2018).
66. I. Stamenkovic, Extracellular matrix remodelling: the role of matrix metalloproteinases. *J. Pathol.* **200**, 448–464 (2003).
67. T. Ching, *et al.*, TapeTech microfluidic connectors: adhesive tape-enabled solution for organ-on-a-chip system integration. (2025). https://doi.org/10.1039/D4LC00970C.
68. Z. Püspöki, M. Storath, D. Sage, M. Unser, “Transforms and Operators for Directional Bioimage Analysis: A Survey” in *Focus on Bio-Image Informatics*, W. H. De Vos, S. Munck, J.-P. Timmermans, Eds. (Springer International Publishing, 2016), pp. 69–93.
69. C. Hajal, *et al.*, Engineered human blood–brain barrier microfluidic model for vascular permeability analyses. *Nat. Protoc.* **17**, 95–128 (2022).

Figures

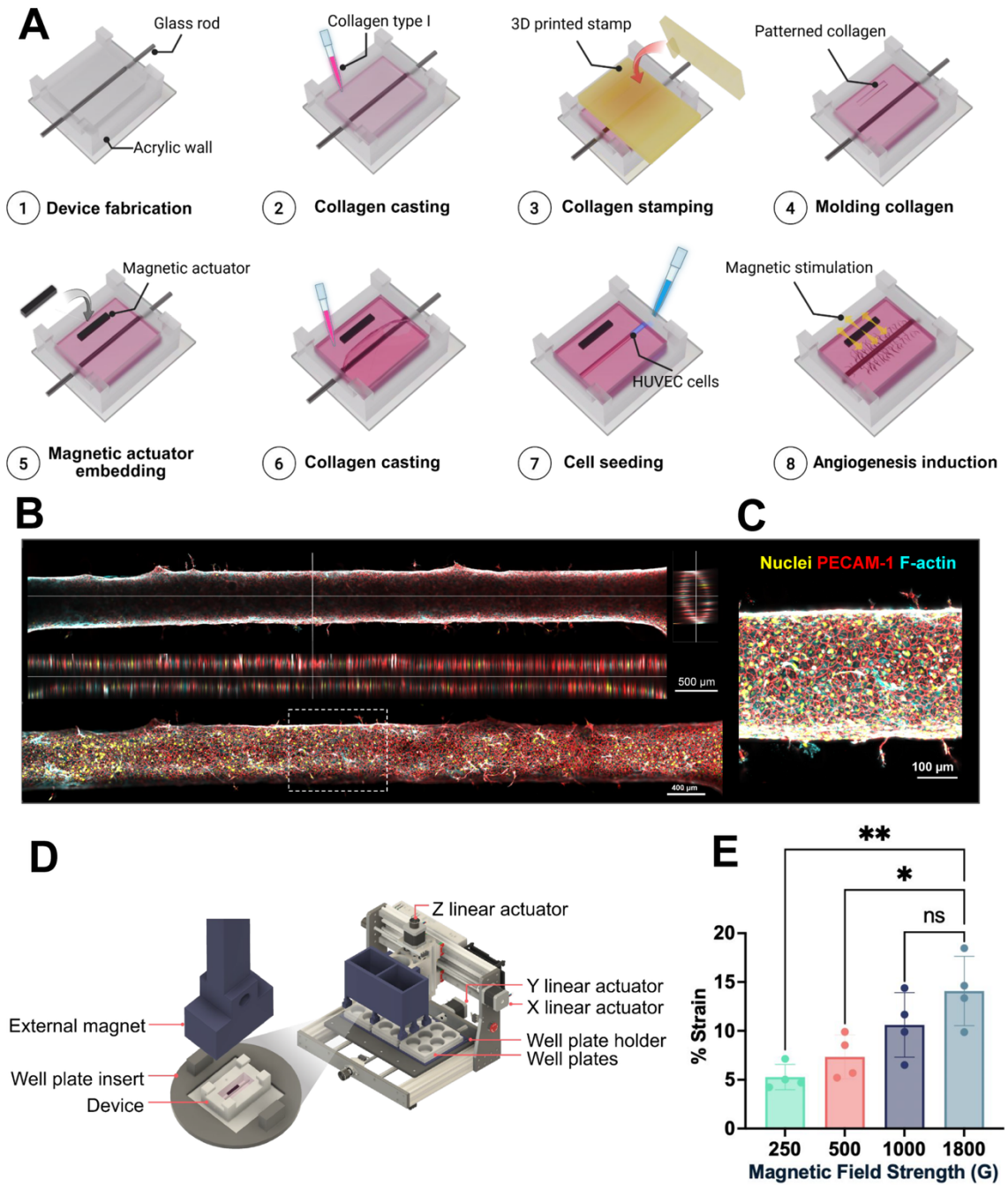

Figure 1. Development of a magnetically actuated vessel-on-chip model for mechanical modulation of angiogenesis. (*A*) Schematic workflow of vessel-on-a-chip device and magnetic actuator integration. A glass rod was inserted into the mold to define a central lumen within a type I collagen matrix (steps 1–2). A 3D-printed stamp was used to create a slot for reproducible positioning of the magnetic actuator (steps 3–4). The magnetic actuator was embedded adjacent to the lumen and encapsulated with an additional collagen layer (steps 5–6). Human umbilical vein endothelial cells (HUVECs) were seeded into the channel to form a confluent endothelium within 48 h (step 7).

Controlled dynamical stimulation was then applied using an external permanent magnet (step 8). (*B*) Representative confocal microscopy images of the unstimulated engineered endothelialized microchannel stained with nuclei (yellow), PECAM-1 (red), and F-actin (cyan). Orthogonal views (vertical and horizontal cross-sections) demonstrate the hollow lumen structure and complete endothelial lining of the vessel. Scale bar is 500 μm. Stitched z-stack maximum projection shows the full extent and three-dimensional organization of the vascular structure. Scale bar is 400 μm. (*C*) High-magnification confocal image of an unstimulated endothelialized microchannel stained for nuclei (yellow), PECAM-1 (red), and F-actin (cyan). Early sprouting extensions are observed protruding from the main vessel into the surrounding collagen matrix. Scale bar is 100 μm. (*D*) Schematic of the automated magnetic actuation platform. The vessel-on-a-chip device is housed within a custom well-plate insert positioned beneath an array of external permanent magnets. Magnet motion is precisely controlled by a motorized XYZ linear actuator assembly, enabling programmable, multidirectional magnetic stimulation across multiple wells for high-throughput mechanical testing. (*E*) Magnetic field strength modulates mechanical strain at the vessel wall. Quantified strain magnitudes at 250, 500, 1,000, and 1,800 G demonstrate precise and tunable mechanical stimulation. The data are shown as mean ± SD ($^{ns}p > 0.05$, $^{*}p < 0.05$, $^{**}p < 0.01$, one-way ANOVA, n=4).

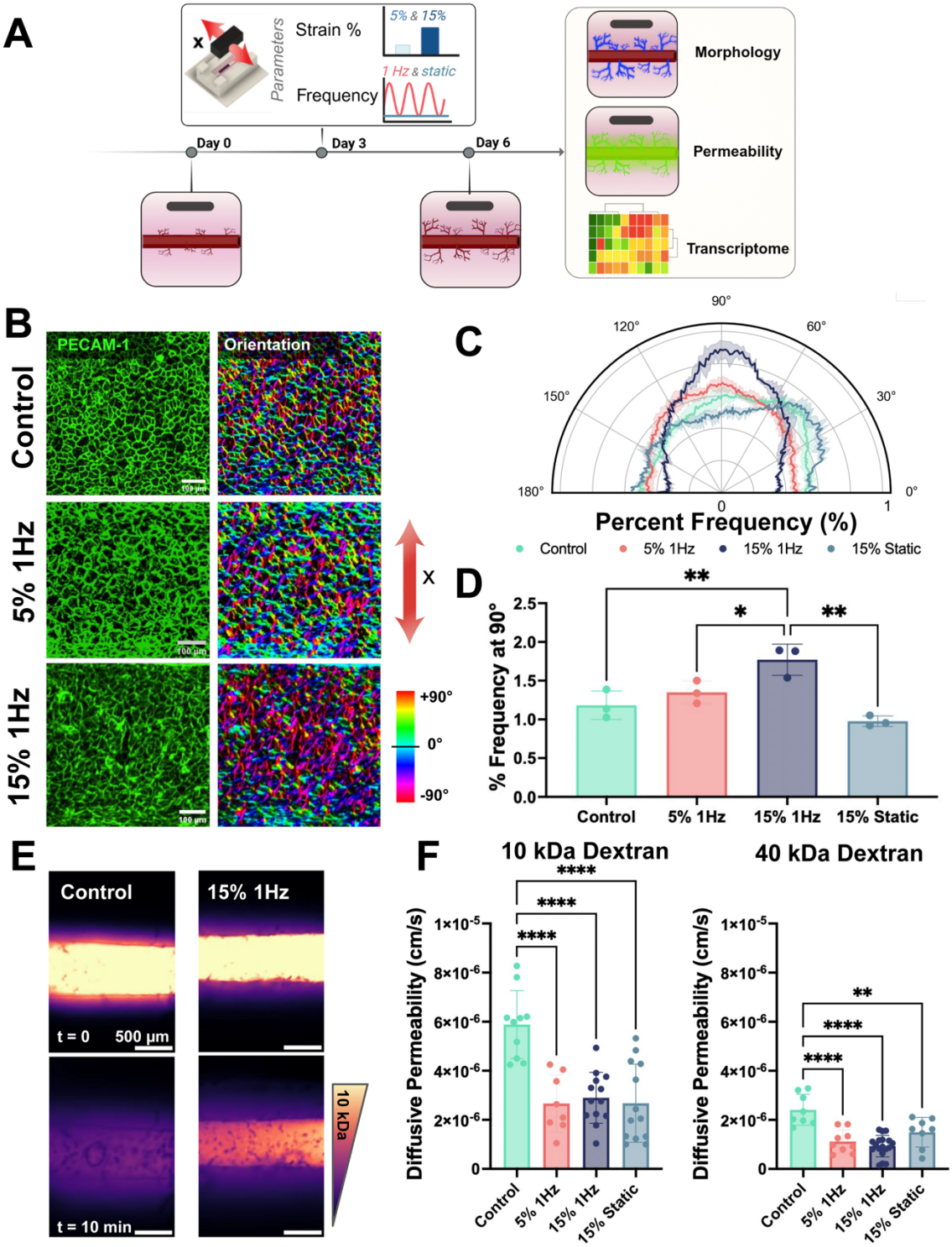

Figure 2. Dynamic mechanical stimulation modulate endothelial cells alignment and barrier properties in 3D vessel-on-a-chip constructs. (*A*) Overview of experimental timeline showing the application of dynamic or static mechanical stimulation (5% or 15%) to engineered vessels starting on day 3. Vessel morphology, permeability, and transcriptomic profiling were assessed after 3 days of stimulation (day 6). (*B*) Representative confocal images showing PECAM-1 staining (green) and

orientation maps of endothelial networks under control, 5% 1 Hz, and 15% 1 Hz strain conditions in the parent vessel. Orientation analysis was performed using OrientationJ, with color coding indicating alignment relative to the stretch axis. Scale bar is 100 µm. (*C*) Polar plots showing the percentage of cells oriented at each angle relative to the strain axis, quantified using OrientationJ. Plots correspond to control, 5% dynamic, 15% dynamic, and 15% static strain conditions, revealing enhanced alignment along the strain axis with increasing dynamic strain magnitude, indicating strain-responsive endothelial reorganization. Shaded regions indicate the standard deviation across biological replicates (n=3). (*D*) Quantification of cell alignment frequency at 90°, corresponding to the direction of applied strain. Dynamic strain induced a significant increase in the proportion of cells aligned along the strain axis, with the highest alignment observed under 15% dynamic stimulation. The data are shown as mean ± SD ($^{ns}p > 0.05$, $^{*}p < 0.05$, $^{**}p < 0.01$, one-way ANOVA, n=3) (*E*) Representative fluorescence images showing diffusion of a fluorescent tracer (10kDa Dextran) across the endothelial barrier at t = 0 (top row) and t = 10 min (bottom row). Control unstimulated vessels show rapid tracer efflux from the vessel lumen into the surrounding matrix, while mechanical strain (15% 1 Hz) significantly restricts tracer leakage, indicating strain-induced enhancement of endothelial barrier integrity. Scale bar is 500 µm. (*F*) Quantification of vessel permeability for 10 kDa and 40 kDa dextran tracers under unstimiulated (control) and stimulated conditions. Both tracer sizes showed reduced permeability under strain (5%, 15% at 1 Hz, and 15% static) compared to unstimulated controls, indicating strain-induced tightening of the endothelial barrier. The data are shown as mean ± SD ($^{ns}p > 0.05$, $^{*}p < 0.05$, $^{**}p < 0.01$, $^{***}p < 0.001$, $^{****}p < 0.0001$, one-way ANOVA, n≥8).

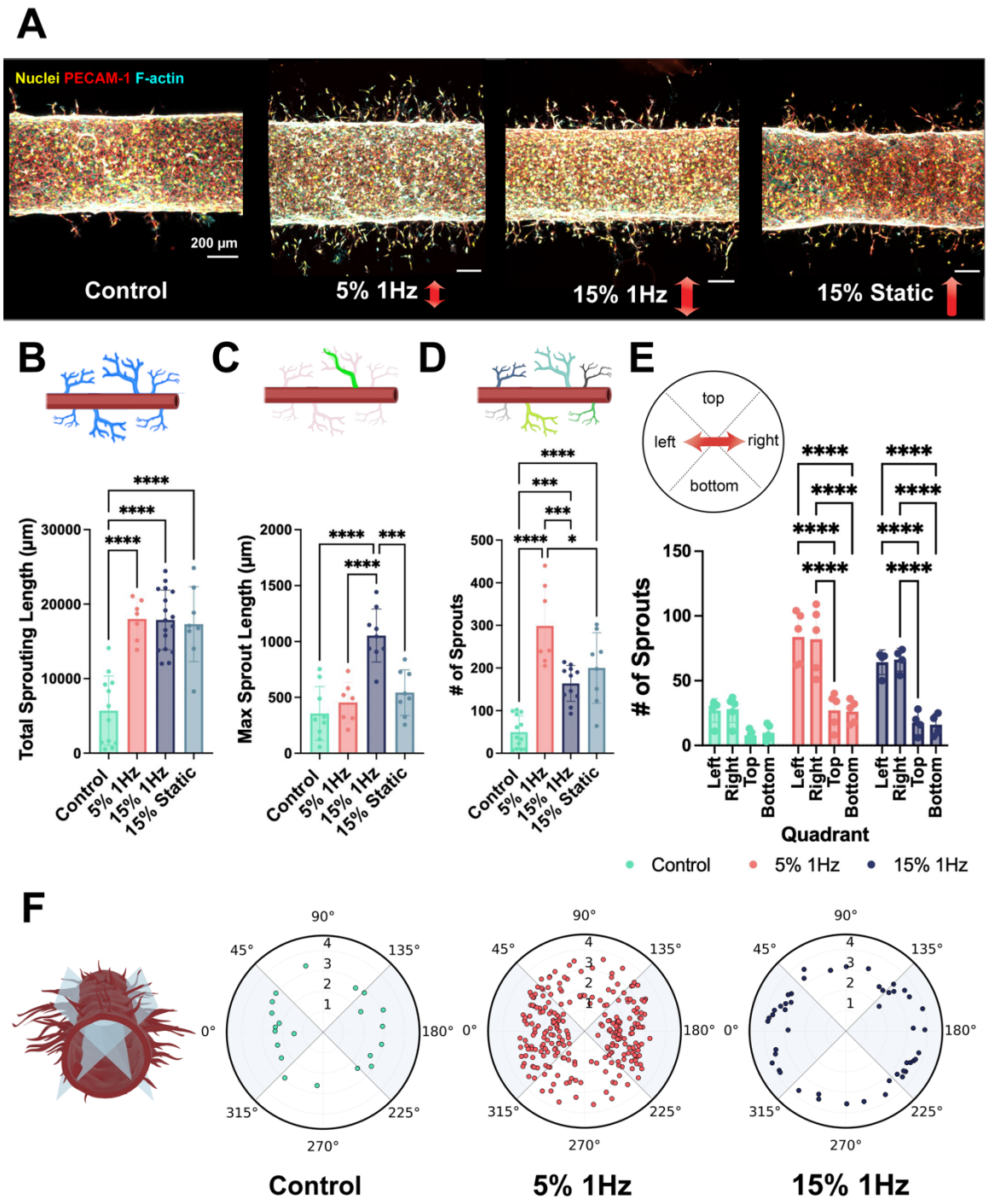

Figure 3. Mechanical strain stimulates angiogenic sprouting and directional vessel branching. (*A*) Representative confocal images of engineered vessels stained for nuclei (DAPI, yellow), PECAM-1 (cell–cell junctions, red), and F-actin (cytoskeleton, cyan) under control (unstimulated), 5% 1Hz, 15% 1Hz, and 15% static strain conditions. Scale bar is 200 µm. (*B*) Quantification of total sprouting length from the parent vessel under control (unstimulated) and strained conditions. Mechanical stimulation significantly increases formation of sprouting compared to unstimulated condition. The data are shown as mean ± SD ($^{ns}p > 0.05$, $^{*}p < 0.05$, $^{**}p < 0.01$, $^{***}p < 0.001$, $^{****}p < 0.0001$, one-

way ANOVA, n≥7) (*C*) Quantification of maximum individual sprout length from the parent vessel under control (unstimulated) and strained conditions. Dynamic stimulation (15% at 1 Hz) produced the longest sprouts, reflecting strain-magnitude–dependent extension of angiogenic branches. The data are shown as mean ± SD ($^{ns}p > 0.05$, $^{*}p < 0.05$, $^{**}p < 0.01$, $^{***}p < 0.001$, $^{****}p < 0.0001$, one-way ANOVA, n≥7) (*D*) Quantification of the number of angiogenic sprouts extending from the parent vessel. 5% dynamic strain significantly increased the number of sprouts compared to unstimulated control. The data are shown as mean ± SD ($^{ns}p > 0.05$, $^{*}p < 0.05$, $^{**}p < 0.01$, $^{***}p < 0.001$, $^{****}p < 0.0001$, one-way ANOVA, n≥7) (*E*) Spatial distribution of sprouts across vessel quadrants (left, right, top, bottom) for control, 5% dynamic, and 15% dynamic strain conditions. Quadrants were defined by dividing the vessel cross-section using angular boundaries at 45°, 135°, 225°, and 315°. ($^{ns}p > 0.05$, $^{*}p < 0.05$, $^{**}p < 0.01$, $^{***}p < 0.001$, $^{****}p < 0.0001$, two-way ANOVA, n≥4). (*F*) Representative rosette plots showing the orientation (θ) and length ($\log_{10}$-transformed) of individual sprouts from one region of interest (ROI) under control, 5% 1 Hz, and 15% 1 Hz strain conditions. Each point corresponds to a single sprout. Shaded quadrants indicate regions aligned with the applied strain axis.

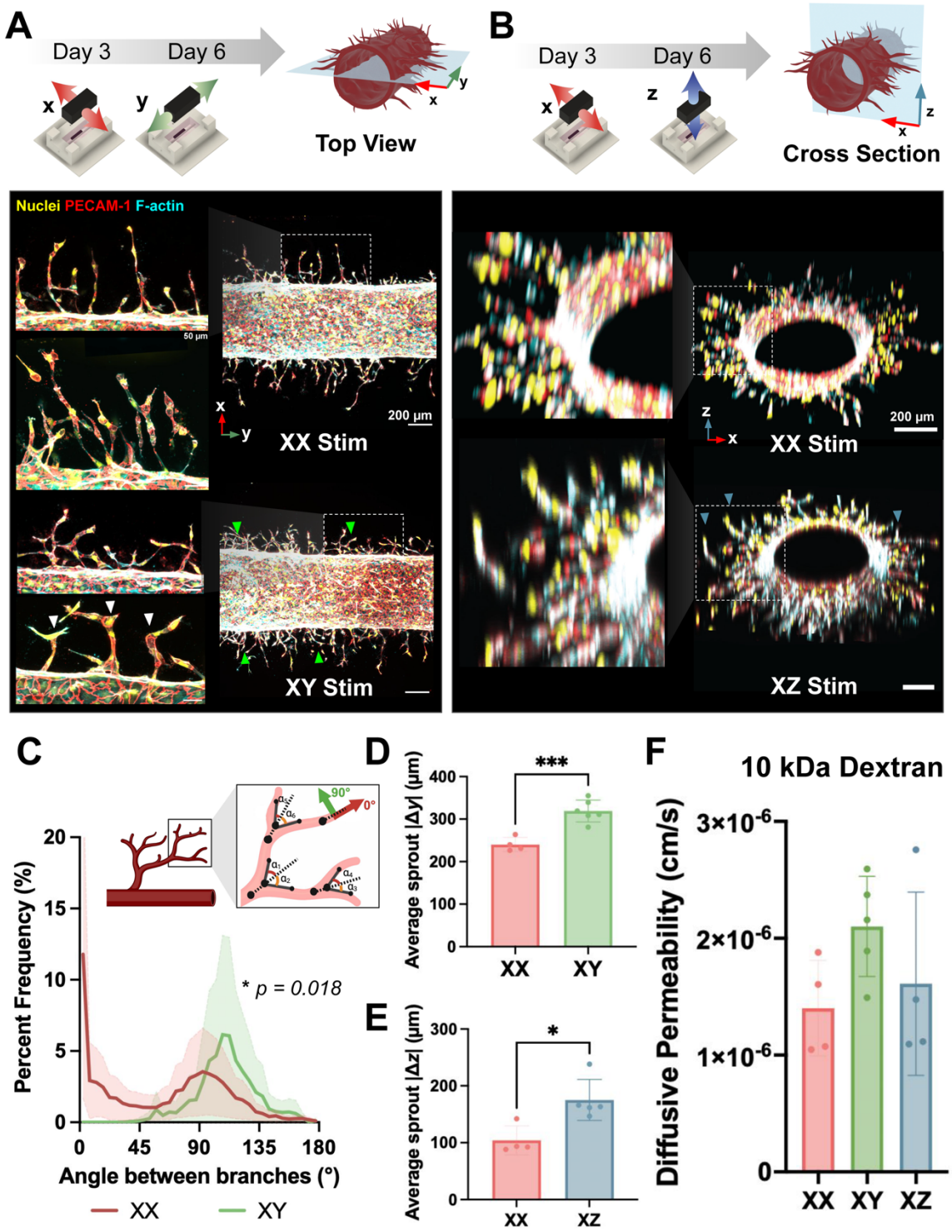

Figure 4. Dynamic reorientation of strain alters endothelial sprouting trajectory across spatial dimensions (*A*) Top-down 3D reconstructions of engineered vessels showing sprouting morphology under XX (x-axis strain maintained for 6 days) and XY (x-axis strain for 3 days followed by y-axis strain for 3 days) stimulation. Green arrows indicate deflection of sprouts along the y-direction under XY stimulation. Scale bars: 200 µm (large images), 50 µm (insets). (*B*) Cross-sectional 3D

reconstructions of engineered vessels under XX and XZ (x-axis strain for 3 days followed by z-axis strain for 3 days) stimulation. Blue arrows indicate upward sprout extension along the z-axis under XZ stimulation. Scale bars: 200 μm (large images) (*C*) Distribution of branch angles measured between parent and daughter branches under XX and XY stimulation. The initial sprout from the parent vessel serves as the reference, and the angles of subsequent branches were analyzed. Distributions were compared using the ($p = 0.018$, Kolmogorov–Smirnov test, $n \geq 3$). (*D*) Quantification of absolute change in y-position ($|\Delta y|$) per sprout under XX and XY stimulation. ($^{ns}p > 0.05$, $^{*}p < 0.05$, $^{**}p < 0.01$, $^{***}p < 0.001$, Unpaired t-test, $n \geq 4$). (*E*) Quantification of absolute change in z-position ($|\Delta z|$) per sprout under XX and XZ stimulation ($^{ns}p > 0.05$, $^{*}p < 0.05$, $^{**}p < 0.01$, Unpaired t-test, $n \geq 4$). (*F*) Diffusive permeability (cm/s) of vessels under XX, XY, and XZ stimulation measured using 10 kDa fluorescent dextran ($^{ns}p > 0.05$, one-way ANOVA, $n \geq 4$).

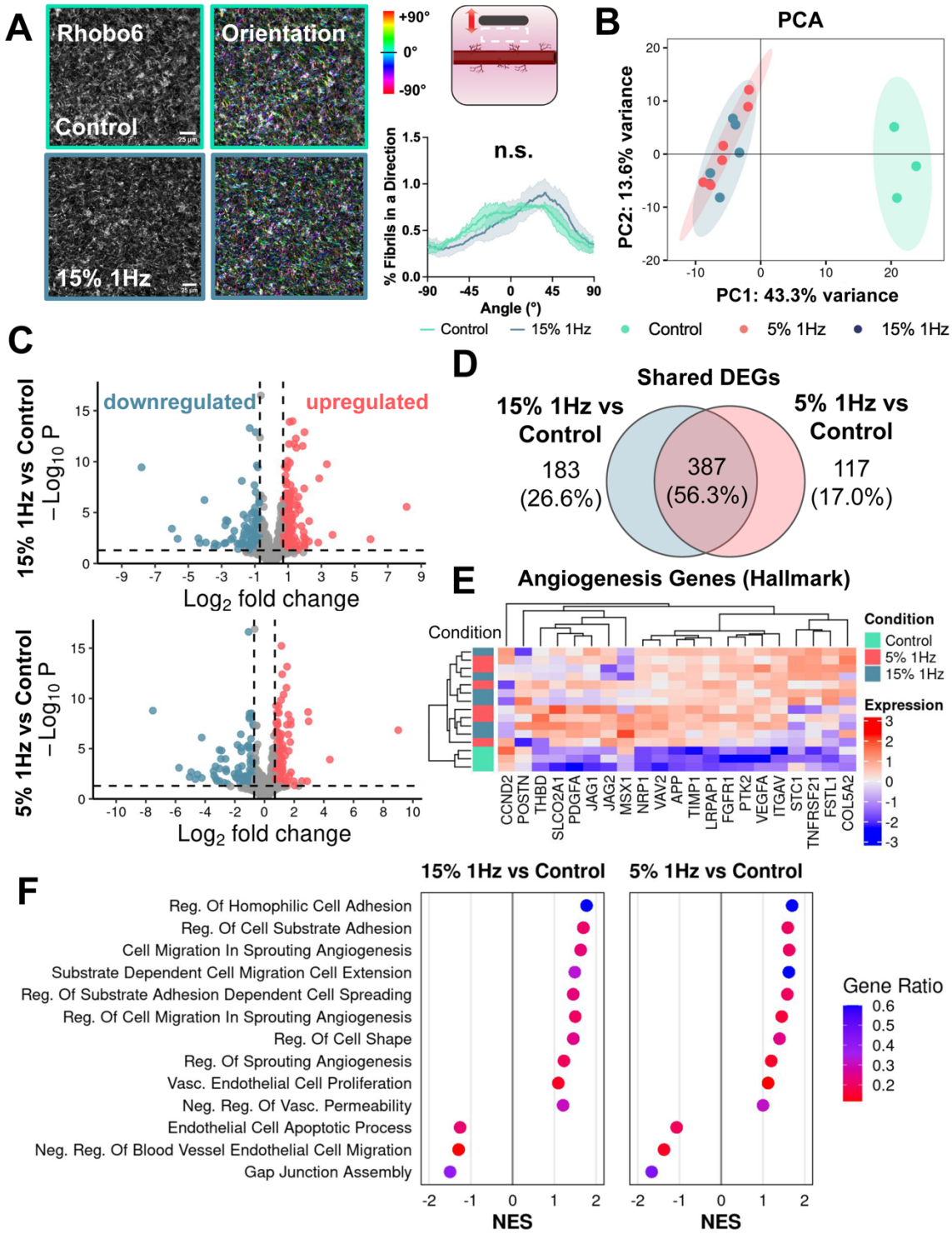

Figure 5. Transcriptomic analysis of endothelial response to mechanical strain (*A*) Collagen fibers visualized using the Rhobo6 fluorescent ECM-binding probe under unstimulated (0% strain) and dynamically actuated (15% 1Hz) conditions. Quantification of collagen fiber orientation was performed across 5 regions of interest per group ($^{ns}p > 0.05$, Unpaired t-test, n=5). (*B*) Principal component analysis (PCA) of bulk RNA-seq samples from unstimulated control, 5% 1Hz, and 15%

1Hz strain conditions. The strain groups (5% 1Hz and 15% 1Hz) had 5 samples with 2 pooled biological replicates per sample. The control group had 3 samples with 2 pooled biological replicates per sample. (*C*) Volcano plots showing upregulated (red) and downregulated (blue) differentially expressed genes (adjusted $p < 0.05$, $|\log_2 \text{ fold change}| > 0.7$) for 15% 1Hz (top) and 5% 1Hz (bottom) relative to control. (*D*) Venn diagrams showing the overlap of differentially expressed genes between 5% 1Hz vs control and 15% 1Hz vs control comparisons. (*E*) Hierarchical clustering heatmap of Hallmark angiogenesis genes across unstimulated control, 5% 1Hz, and 15% 1Hz samples. (*F*) Gene set enrichment analysis (GSEA) of biological processes across strain conditions, ranked by normalized enriched score (NES).